

1

²A SEARCH FOR LONG-LIVED, CHARGED, SUPERSYMMETRIC PARTICLES
³USING IONIZATION WITH THE ATLAS DETECTOR

4

BRADLEY AXEN

5

September 2016 – Version 0.19

6



⁸ Bradley Axen: *A Search for Long-Lived, Charged, Supersymmetric Particles using Ion-
⁹ ization with the ATLAS Detector*, Subtitle, © September 2016

10

Usually a quotation.

11

Dedicated to.

₁₂ ABSTRACT

₁₃ How to write a good abstract:

₁₄ <https://plg.uwaterloo.ca/~migod/research/beck00PSLA.html>

₁₅ PUBLICATIONS

₁₆ Some ideas and figures have appeared previously in the following publications:

₁₇

₁₈ Put your publications from the thesis here. The packages `multibib` or `bibtopic`
₁₉ etc. can be used to handle multiple different bibliographies in your document.

²¹ ACKNOWLEDGEMENTS

²² Put your acknowledgements here.

²³

²⁴ And potentially a second round.

²⁵

26 CONTENTS

27	I	INTRODUCTION	1
28	1	INTRODUCTION	3
29	II	THEORETICAL CONTEXT	5
30	2	STANDARD MODEL	7
31	2.1	Particles	7
32	2.2	Interactions	8
33	2.3	Limitations	8
34	3	SUPERSYMMETRY	9
35	3.1	Motivation	9
36	3.2	Structure	9
37	3.3	Phenomenology	9
38	4	LONG-LIVED PARTICLES	11
39	4.1	Mechanisms	11
40	4.1.1	Examples in Supersymmetry	11
41	4.2	Phenomenology	11
42	4.2.1	Disimilarities to Prompt Decays	11
43	4.2.2	Characteristic Signatures	11
44	III	EXPERIMENTAL STRUCTURE AND RECONSTRUCTION	13
45	5	THE LARGE HADRON COLLIDER	15
46	5.1	Injection Chain	15
47	5.2	Design and Parameters	15
48	5.3	Luminosity	15
49	6	THE ATLAS DETECTOR	17
50	6.1	Coordinate System	17
51	6.2	Magnetic Field	17
52	6.3	Inner Detector	17
53	6.3.1	Pixel Detector	17
54	6.3.2	Semiconductor Tracker	17
55	6.3.3	Transition Radiation Tracker	17
56	6.4	Calorimetry	17
57	6.4.1	Electromagnetic Calorimeters	17
58	6.4.2	Hadronic Calorimeters	17
59	6.4.3	Forward Calorimeters	17
60	6.5	Muon Spectrometer	17
61	6.6	Trigger	17
62	6.6.1	Trigger Scheme	17
63	6.6.2	Missing Transverse Energy Triggers	17
64	7	EVENT RECONSTRUCTION	19
65	7.1	Tracks and Vertices	19

66	7.1.1	Track Reconstruction	19
67	7.1.2	Vertex Reconstruction	19
68	7.2	Jets	19
69	7.2.1	Topological Clustering	19
70	7.2.2	Jet Energy Scale	19
71	7.2.3	Jet Energy Scale Uncertainties	19
72	7.2.4	Jet Energy Resolution	19
73	7.3	Electrons	19
74	7.3.1	Electron Identification	19
75	7.4	Muons	19
76	7.4.1	Muon Identification	19
77	7.5	Missing Transverse Energy	19
78	IV	CALORIMETER RESPONSE	21
79	8	RESPONSE MEASUREMENT WITH SINGLE HADRONS	23
80	8.1	Dataset and Simulation	24
81	8.1.1	Data Samples	24
82	8.1.2	Simulated Samples	24
83	8.1.3	Event Selection	24
84	8.2	Inclusive Hadron Response	25
85	8.2.1	E/p Distribution	25
86	8.2.2	Zero Fraction	26
87	8.2.3	Neutral Background Subtraction	28
88	8.2.4	Corrected Response	28
89	8.3	Identified Particle Response	33
90	8.3.1	Decay Reconstruction	33
91	8.3.2	Identified Response	34
92	8.3.3	Additional Species in Simulation	35
93	8.4	Summary	36
94	9	JET ENERGY RESPONSE AND UNCERTAINTY	39
95	9.1	Jet Composition	39
96	9.2	Uncertainty Estimate	39
97	9.3	Summary	42
98	V	SEARCH FOR LONG-LIVED PARTICLES	43
99	10	LONG-LIVED PARTICLES IN ATLAS	45
100	10.1	Overview and Characteristics	45
101	10.2	Simulation	45
102	11	EVENT SELECTION	47
103	11.1	Trigger	47
104	11.2	Kinematics and Isolation	47
105	11.3	Standard Model Rejection	47
106	11.4	Ionization	47
107	11.4.1	dE/dx Calibration	47
108	11.4.2	Mass Estimation	47
109	12	BACKGROUND ESTIMATION	49

110	12.1	Background Sources	49
111	12.2	Prediction Method	49
112	12.3	Validation and Uncertainty	49
113	13	SYSTEMATIC UNCERTAINTIES AND RESULTS	51
114	13.1	Systematic Uncertainties	51
115	13.2	Final Yields	51
116	14	INTERPRETATION	53
117	14.1	Cross Sectional Limits	53
118	14.2	Mass Limits	53
119	14.3	Context for Long-Lived Searches	53
120	VI	CONCLUSIONS	55
121	15	SUMMARY AND OUTLOOK	57
122	15.1	Summary	57
123	15.2	Outlook	57
124	VII	APPENDIX	59
125	A	INELASTIC CROSS SECTION	61
126	B	APPENDIX TEST	63
127	B.1	Appendix Section Test	63
128	B.1.1	Appendix Subection Test	63
129	B.2	A Table and Listing	63
130	B.3	Some Formulas	64
131		BIBLIOGRAPHY	67

132 LIST OF FIGURES

133	Figure 1	The particle content of the Standard Model.	8
134	Figure 2	An illustration (a) of the E/p variable used throughout this paper. The red energy deposits come from the charged particle targeted for measurement, while the blue energy deposits are from nearby neutral particles and must be subtracted. The same diagram (b) for the neutral-background selection, described in Section 8.2.3.	26
135			
136			
137			
138			
139			
140	Figure 3	The E/p distribution and ratio of simulation to data for isolated tracks with (a) $ \eta < 0.6$ and $1.2 < p/\text{GeV} < 1.8$ and (b) $ \eta < 0.6$ and $2.2 < p/\text{GeV} < 2.8$	26
141			
142			
143	Figure 4	The fraction of tracks as a function (a, b) of momentum, (c, d) of interaction lengths with $E \leq 0$ for tracks with positive (on the left) and negative (on the right) charge.	27
144			
145			
146			
147	Figure 5	$\langle E/p \rangle_{\text{BG}}$ as a function of the track momentum and (a) $ \eta < 0.6$, (b) $0.6 < \eta < 1.1$, and as a function of the track pseudorapidity and (c) $1.2 < p/\text{GeV} < 1.8$, (d) $1.8 < p/\text{GeV} < 2.2$	29
148			
149			
150			
151	Figure 6	$\langle E/p \rangle_{\text{COR}}$ as a function of track momentum, for tracks with (a) $ \eta < 0.6$, (b) $0.6 < \eta < 1.1$, (c) $1.8 < \eta < 1.9$, and (d) $1.9 < \eta < 2.3$	30
152			
153			
154	Figure 7	$\langle E/p \rangle_{\text{COR}}$ calculated using LCW-calibrated topological clusters as a function of track momentum for tracks with (a) zero or more associated topological clusters or (b) one or more associated topological clusters.	31
155			
156			
157			
158	Figure 8	Comparison of the $\langle E/p \rangle_{\text{COR}}$ for tracks with (a) less than and (b) greater than 20 hits in the TRT.	32
159			
160	Figure 9	Comparison of the $\langle E/p \rangle_{\text{COR}}$ for (a) positive and (b) negative tracks as a function of track momentum for tracks with $ \eta < 0.6$	32
161			
162			
163	Figure 10	Comparison of the E/p distributions for (a) positive and (b) negative tracks with $0.8 < p/\text{GeV} < 1.2$ and $ \eta < 0.6$, in simulation with the FTFP_BERT and QGSP_BERT physics lists.	33
164			
165			
166			
167	Figure 11	The reconstructed mass peaks of (a) K_S^0 , (b) Λ , and (c) $\bar{\Lambda}$ candidates.	34
168			
169	Figure 12	The E/p distribution for isolated (a) π^+ , (b) π^- , (c) proton, and (d) anti-proton tracks.	35
170			
171	Figure 13	The fraction of tracks with $E \leq 0$ for identified (a) π^+ and π^- , and (b) proton and anti-proton tracks	36
172			

173 Figure 14	The difference in $\langle E/p \rangle$ between (a) π^+ and π^- (b) p and π^+ , and (c) \bar{p} and π^-	37
174 Figure 15	$\langle E/p \rangle_{\text{COR}}$ as a function of track momentum for (a) π^+ tracks and (b) π^- tracks.	37
175 Figure 16	The ratio of the calorimeter response to single particles of various species to the calorimeter response to π^+ with the physics list FTFP_BERT.	37
176 Figure 17	The spectra of true particles inside anti- k_t , $R = 0.4$ jets with (a) $90 < p_T/\text{GeV} < 100$, (b) $400 < p_T/\text{GeV} < 500$, and (c) $1800 < p_T/\text{GeV} < 2300$	40
177 Figure 18	The jet energy scale uncertainty contributions, as well as the total jet energy scale uncertainty, as a function of jet p_T for (a) $ \eta < 0.6$ and (b) $0.6 < \eta < 1.1$	41
178 Figure 19	The jet energy scale correlations as a function of jet p_T and $ \eta $ for jets in the central region of the detector.	42
179		
180		
181		
182		
183		
184		
185		
186		
187		

¹⁸⁸ LIST OF TABLES

¹⁸⁹ Table 1	Autem usu id	63
------------------------	------------------------	----

₁₉₀ LISTINGS

₁₉₁ Listing 1	A floating example (<code>listings</code> manual)	64
--------------------------	--	----

192 ACRONYMS

193 EG Example

194

PART I

195

INTRODUCTION

196

You can put some informational part preamble text here.

1

197

198 INTRODUCTION

199

PART II

200

THEORETICAL CONTEXT

201

You can put some informational part preamble text here.

2

202

203 STANDARD MODEL

204 The Standard Model of particle physics seeks to explain the symmetries and in-
205 teractions of all currently discovered fundamental particles. It has been tested by
206 several generations of experiments and has been remarkably successful, no sig-
207 nificant deviations have been found. The Standard Model provides predictions
208 in particle physics for interactions up to the Planck scale (10^{15} - 10^{19} GeV).

209 The theory itself is a quantum field theory grown from an underlying $SU(3) \times$
210 $SU(2) \times U(1)$ that requires the particle content and quantum numbers consist-
211 ent with experimental observations (see Section 2.1). Each postulated symme-
212 try is accompanied by an interaction between particles through gauge invari-
213 ance. These interactions are referred to as the Strong, Weak, and Electromag-
214 netic forces, which are discussed in Section 2.2.

215 Although this model has been very predictive, the theory is incomplete; for
216 example, it is not able to describe gravity or astronomically observed dark matter.
217 These limitations are discussed in more detail in Section 2.3.

218 21 PARTICLES

219 The most familiar matter in the universe is made up of protons, neutrons, and
220 electrons. Protons and neutrons are composite particles, however, and are made
221 up in turn by particles called quarks. Quarks carry both electric charge and color
222 charge, and are bound in color-neutral combinations called baryons. The elec-
223 tron is an example of a lepton, and carries only electric charge. Another type
224 of particle, the neutrino, does not form atomic structures in the same way that
225 quarks and leptons do because it carries no color or electric charge. Collectively,
226 these types of particles are known as fermions, the group of particles with half-
227 integer spin.

228 There are three generations of fermions, although familiar matter is formed
229 predominantly by the first generation. The generations are identical except for
230 their masses, which increase in each generation by convention. In addition, each
231 of these particles is accompanied by an antiparticle, with opposite-sign quantum
232 numbers but the same mass.

233 The fermions comprise what is typically considered matter, but there are
234 additional particles that are mediators of interactions between those fermions.
235 These mediators are known as the gauge bosons, gauge in that their existence
236 is required by gauge invariance (discussed further in Section 2.2) and bosons in
237 that they have integer spin. The boson which mediates the electromagnetic force
238 is the photon, the first boson to be discovered; it has no electric charge, no mass,
239 and a spin of 1. There are three spin-1 mediators of the weak force, the two W
240 bosons and the Z boson. The W bosons have electric charge of ± 1 and a mass of
241 80.385 ± 0.015 GeV, while the Z boson is neutral and has a mass of $91.1876 \pm$

242 0.0021 GeV. The strong force is mediated by eight particles called gluons, which
 243 are massless and electrically neutral but do carry color charge.

244 The final particle present in the Standard Model is the Higgs boson, which was
 245 recently observed for the first time by experiments at CERN in 2012. It is electric-
 246 cally neutral, has a mass of 125.7 ± 0.4 GeV, and is the only spin-0 particle yet to
 247 be observed. The Higgs boson is the gauge boson associated with the mechanism
 248 that gives a mass to the W and Z bosons.

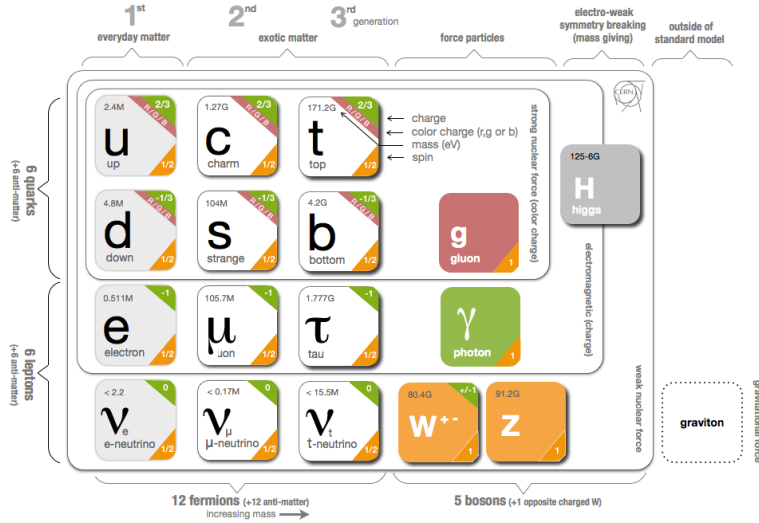


Figure 1: The particle content of the Standard Model.

249 Together these particles form the entire content of the Standard Model, and
 250 are summarized in Figure 1. These are the particles that constitute the observable
 251 universe and all the so-far-observed interactions within it.

2.2 INTERACTIONS

253 The interactions predicted and described by the Standard Model are fundamen-
 254 tally tied to the particles within it, both in that they describe the way those par-
 255 ticles can influence each other and also in that the existence of the interactions
 256 requires the existence of some particles (the gauge bosons).

2.3 LIMITATIONS

3

258

259 SUPERSYMMETRY

260 3.1 MOTIVATION

261 3.2 STRUCTURE

262 3.3 PHENOMENOLOGY

4

263

264 LONG-LIVED PARTICLES

265 4.1 MECHANISMS

266 4.1.1 EXAMPLES IN SUPERSYMMETRY

267 4.2 PHENOMENOLOGY

268 4.2.1 DISIMILARITIES TO PROMPT DECAYS

269 4.2.2 CHARACTERISTIC SIGNATURES

EXPERIMENTAL STRUCTURE AND RECONSTRUCTION

You can put some informational part preamble text here.

5

273

274 THE LARGE HADRON COLLIDER

275 5.1 INJECTION CHAIN

276 5.2 DESIGN AND PARAMETERS

277 5.3 LUMINOSITY

6

278

279 THE ATLAS DETECTOR

280 6.1 COORDINATE SYSTEM

281 6.2 MAGNETIC FIELD

282 6.3 INNER DETECTOR

283 6.3.1 PIXEL DETECTOR

284 6.3.2 SEMICONDUCTOR TRACKER

285 6.3.3 TRANSITION RADIATION TRACKER

286 6.4 CALORIMETRY

287 6.4.1 ELECTROMAGNETIC CALORIMETERS

288 6.4.2 HADRONIC CALORIMETERS

289 6.4.3 FORWARD CALORIMETERS

290 6.5 MUON SPECTROMETER

291 6.6 TRIGGER

292 6.6.1 TRIGGER SCHEME

293 6.6.2 MISSING TRANSVERSE ENERGY TRIGGERS

7

294

295 EVENT RECONSTRUCTION

296 The ATLAS experiment combines measurements in the subdetectors to form a
297 cohesive picture of each physics event.

298 7.1 TRACKS AND VERTICES

299 7.1.1 TRACK RECONSTRUCTION

300 7.1.1.1 NEURAL NETWORK

301 7.1.1.2 PIXEL DE/DX

302 7.1.2 VERTEX RECONSTRUCTION

303 7.2 JETS

304 7.2.1 TOPOLOGICAL CLUSTERING

305 7.2.2 JET ENERGY SCALE

306 7.2.3 JET ENERGY SCALE UNCERTAINTIES

307 7.2.4 JET ENERGY RESOLUTION

308 7.3 ELECTRONS

309 7.3.1 ELECTRON IDENTIFICATION

310 7.4 MUONS

311 7.4.1 MUON IDENTIFICATION

312 7.5 MISSING TRANSVERSE ENERGY

313

PART IV

314

CALORIMETER RESPONSE

315

You can put some informational part preamble text here.

318 As discussed in Section 7.2, colored particles produced in collisions hadronize
319 into jets of multiple individual hadrons. As jets form a major component of many
320 physics analyses at ATLAS, it is crucial to carefully calibrate the measurement of
321 jet energies and to derive an uncertainty on that measurement. These uncertain-
322 ties have often been the dominant systematic uncertainty in high-energy analy-
323 ses at the LHC.

324 One approach to understanding jet physics in the ATLAS calorimetry is to
325 evaluate the calorimeter response to individual hadrons; measurements of indi-
326 vidual hadrons can be used to build up an understanding of the jets that they form.
327 The redundancy of the momentum provided by the tracking system and the en-
328 ergy provided by the calorimeter provides an opportunity to study calorimeter
329 response using real collisions, as described further in Section 8.2.

330 A number of interesting factors compromise calorimeter response, and ex-
331 tracting these separately provides insight into many aspects of jet modeling. First,
332 many charged hadrons interact with the material of the detector prior to reach-
333 ing the calorimeters and thus do not deposit any energy. Comparing this effect in
334 data and simulation is a powerful tool in validating the interactions of particles
335 with the material of the detector as well as the model of the detector geometry
336 in simulation, see Section 8.2.2. The particles which do reach the calorimeter de-
337 posit their energy into individual cells, which are then clustered to measure full
338 energy deposits. Comparing the response in data to simulated hadrons provides
339 a direct evaluation of several aspects of simulation: noise in the calorimeters, the
340 showering of hadronic particles, and the energy deposited by particles in mat-
341 ter, among others (Section 8.2.4). These measurements are extended to explore
342 several additional effects, such as the dependence on charge or the individual
343 calorimeter layer in Section 8.2.4.1.

344 The above studies all use an inclusive selection of charged particles, which are
345 compromised predominantly of pions, kaons, and (anti)protons. It is also inter-
346 esting to measure the particle types separately to evaluate the simulated inter-
347 actions of each particle, particularly at low energies where differences between
348 species are very relevant. Pions and (anti)protons can be identified through de-
349 cays of long-lived particles, in particular Λ , $\bar{\Lambda}$, and K_S^0 , and then used to measure
350 response as described above. This is discussed in detail in Section 8.3.

351 Together, these measurements in data provide a thorough understanding of
352 the way hadrons interact with the ATLAS detector and can be used to build up a
353 description of jets, as seen in Chapter 9. The results in this chapter use data col-
354 lected at 7 and 8 TeV collected in 2010 and 2012, respectively. Both are included
355 as the calorimeter was repaired and recalibrated between those two data-taking
356 periods. Both sets of data are compared to an updated simulation that includes
357 new physics models provided by Geant4 [12] and improvements in the detector

358 description [2, 6]. These results are published in EPJC [8] and can be compared to
 359 a similar measurement performed in 2009 and 2010 [5], which used the previous
 360 version of the simulation framework [1].

361 8.1 DATASET AND SIMULATION

362 8.1.1 DATA SAMPLES

363 The two datasets used in this chapter are taken from dedicated low-pileup runs
 364 where the fraction of events with multiple interactions was negligible, to facilitate
 365 measurement of isolated hadrons. The 2012 dataset at $\sqrt{s} = 8$ TeV contains 8
 366 million events and corresponds to an integrated luminosity of 0.1 nb^{-1} . The 2010
 367 dataset at $\sqrt{s} = 7$ TeV contains 3 million events and corresponds to an integrated
 368 luminosity of 3.2 nb^{-1} . This last dataset was also used in the 2010 results [5], but
 369 have since been reanalyzed with an updated detector description of the material
 370 and alignment.

371 8.1.2 SIMULATED SAMPLES

372 The two datasets above are compared to simulated single-, double-, and non-
 373 diffractive events generated with Pythia8 [32] using the A2 configuration of
 374 hadronization [3] and the MSTW 2008 parton-distribution function set [28, 31].
 375 The conditions and energies for each run are matched in the two simulations.

376 To evaluate the interaction of hadrons with detector material, the simulation
 377 uses two different collections of hadronic physics models, called physics lists, in
 378 Geant4 9.4 [30]. The first, QGSP_BERT, combines the Bertini intra-nuclear
 379 cascade [17, 24, 26] below 9.9 GeV, a parametrized proton inelastic model from
 380 9.5 to 25 GeV [21], and a quark-gluon string model above 12 GeV [13, 14, 18, 19,
 381 22]. The second, FTFP_BERT, combines the Bertini intra-nuclear cascade [17, 24,
 382 26] below 5 GeV and the Fritiof model [15, 16, 23, 29] above 4 GeV. In either list,
 383 where multiple models overlap, the transition between the two models is ensured
 384 to be smooth.

385 8.1.3 EVENT SELECTION

386 The event selection for this study is minimal, as the only requirement is selecting
 387 good-quality events with an isolated track. Such events are triggered by requiring
 388 at least two hits in the minimum-bias trigger scintillators. After trigger, each
 389 event is required to have exactly one reconstructed vertex, and that vertex is re-
 390 quired to have four or more associated tracks.

391 The particles which enter into the response measurements are first identified
 392 as tracks in the inner detector. To ensure a reliable momentum measurement,
 393 these tracks are required to have at least one hit in the pixel detector, six hits in
 394 the SCT, and small longitudinal and transverse impact parameters with respect
 395 to the primary vertex [5]. For the majority of the measurements in this chap-

396 ter, the track is additionally required to have 20 hits in the TRT, which signifi-
 397 cantly reduces the contribution from tracks which undergo nuclear interactions.
 398 This requirement and its effect is discussed in more detail in Section 8.2.4.1. In
 399 addition, tracks are rejected if there is another track which extrapolates to the
 400 calorimeter within a cone of $\Delta R = \sqrt{(\Delta\phi)^2 + (\Delta\eta)^2} < 0.4$. This requirement
 401 guarantees that the contamination of energy from nearby charged particles is
 402 negligible [5].

403 8.2 INCLUSIVE HADRON RESPONSE

404 The calorimeter response is more precisely defined as the ratio of the measured
 405 calorimeter energy to the true energy carried by the particle, although this true
 406 energy is unknown. For charged particles, however, the inner detector provides
 407 a very precise measurement of momentum (with uncertainty less than 1%) that
 408 can be used as a proxy for true energy. The ratio of the energy deposited by the
 409 charged particle in the calorimeter, E , to its momentum measured in the inner
 410 detector p , forms the calorimeter response measure called E/p . Though the dis-
 411 tribution of E/p is interesting, two aggregated quantities are more directly use-
 412 ful: $\langle E/p \rangle$, the average of E/p within a given subset of particles, and the zero
 413 fraction, the fraction of particles with no associated clusters in the calorimeter.

414 The calorimeter energy assigned to a track particle is defined using either
 415 clusters. The clusters are formed using a 4–2–0 algorithm [9] that begins with
 416 seeds requiring at least 4 times the calorimeter average noise. The neighboring
 417 cells with at least twice that noise threshold are then added to the cluster, and all
 418 bounding cells are then added with no requirement. This algorithm minimizes
 419 noise contributions through its seeding process, and including the additional lay-
 420 ers improves the energy resolution [33]. The clusters are associated to a given
 421 track if they fall within a cone of $\Delta R = 0.2$ of the extrapolated position of the
 422 track, which includes about 90% of the energy on average [5]. This construction
 423 is illustrated in Figure 2.

424 8.2.1 E/P DISTRIBUTION

425 The E/p distributions measured in both data and simulation are shown in Fig-
 426 ure 3 for two example bins of track momentum and for tracks in the central
 427 region of the detector. These distribution show several important features of
 428 the E/p observable. The large content in the bin at $E = 0$ comes from tracks that
 429 have no associated cluster, as mentioned previously these are due to interactions
 430 with detector material prior to reaching the calorimeter or the energy deposit be-
 431 ing insufficiently large to generate a seed, and are discussed in Section 8.2.2. The
 432 small negative tail comes from similar tracks that do not deposit any energy in
 433 the calorimeter but are randomly associated to a noise cluster. The long positive
 434 tail above 1.0 comes from the contribution of neutral particles. Nearby neutral
 435 particles deposit (sometimes large) additional energy in the calorimeter but do
 436 not produce tracks in the inner detector and so they cannot be rejected for isolat-
 437 tion. Additionally the peak and mean of the distribution falls below 1.0 because

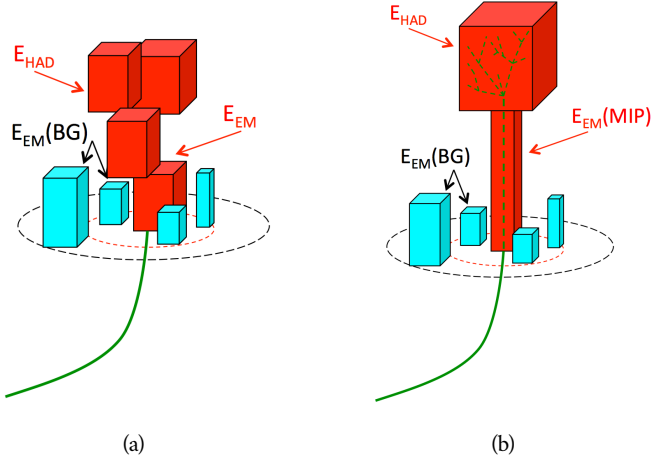


Figure 2: An illustration (a) of the E/p variable used throughout this paper. The red energy deposits come from the charged particle targeted for measurement, while the blue energy deposits are from nearby neutral particles and must be subtracted. The same diagram (b) for the neutral-background selection, described in Section 8.2.3.

438 of the loss of energy not found within the cone as well as the non-compensation
 439 of the calorimeter.

440 The data and simulation share the same features, but the high and low tails
 441 are significantly different. The simulated events tend to overestimate the contri-
 442 bution of neutral particle to the long tail, although this effect can be isolated as
 443 discussed in Section 8.2.3. Additionally, the simulated clusters have less noise on
 444 average, although this is a small effect on the overall response.

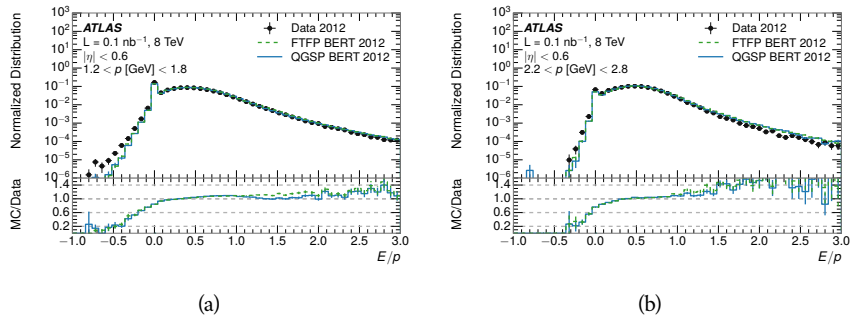


Figure 3: The E/p distribution and ratio of simulation to data for isolated tracks with
 (a) $|\eta| < 0.6$ and $1.2 < p/\text{GeV} < 1.8$ and (b) $|\eta| < 0.6$ and $2.2 < p/\text{GeV} < 2.8$.

445 8.2.2 ZERO FRACTION

446 The fraction of particles with no associated clusters, or similarly those with $E \leq$
 447 0, reflects the modeling of both the detector geometry and hadronic interactions.
 448 The zero fraction is expected to rise as the amount of material a particle traverses

increases, while it is expected to decrease as the particle energy increases. This dependence can be seen in Figure 4, where the zero fraction in data and simulation is shown as a function of momentum and the amount of material measured in interaction lengths. The trends are similar between the 2010 and 2012 measurements. The zero fraction decreases with energy as expected. The amount of material in the detector increases with η , which provides a distribution of interaction lengths. As the data and simulation have significant disagreement in the zero fraction over a number of interaction lengths, the difference must be primarily from the modeling of hadronic interactions with detector material..

There is also a noticeable difference between positive at negative tracks at low momentum, which reflects the difference in response between protons and antiprotons. Antiprotons have significant model differences in the two physics lists, QGSP_BERT and FTFP_BERT, and this is evident in the lowest momentum bin of the data to simulation ratio. This difference is explored further in Section 8.3.

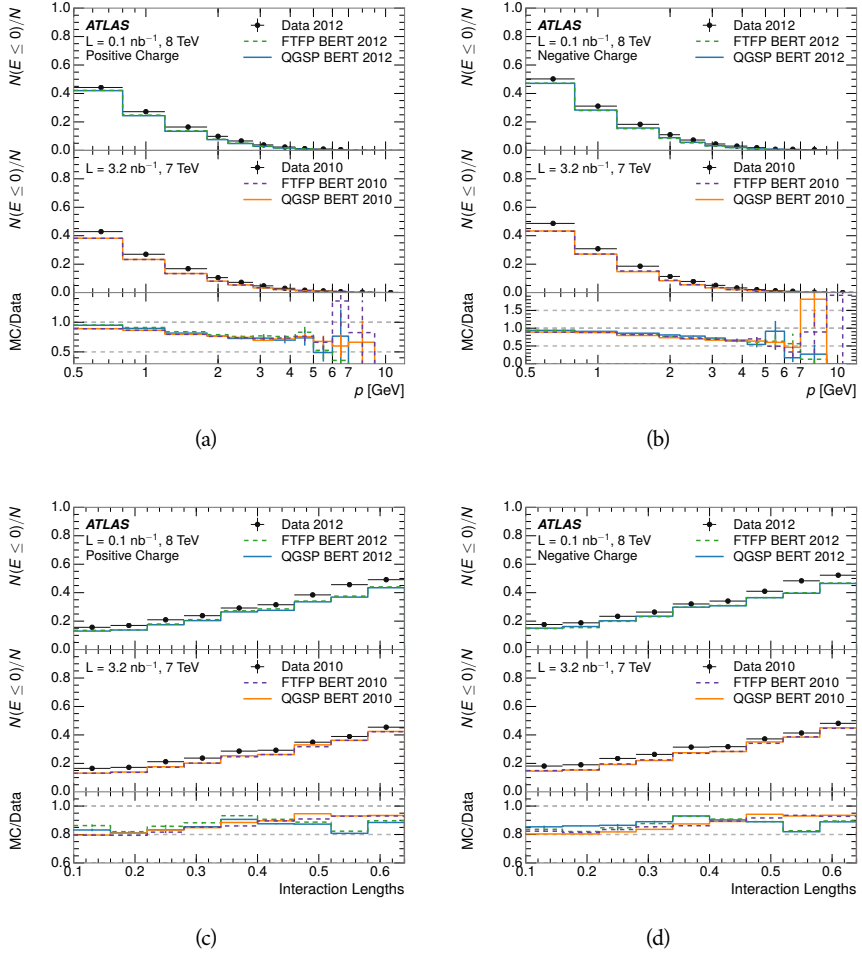


Figure 4: The fraction of tracks as a function (a, b) of momentum, (c, d) of interaction lengths with $E \leq 0$ for tracks with positive (on the left) and negative (on the right) charge.

463 8.2.3 NEUTRAL BACKGROUND SUBTRACTION

464 The isolation requirement on hadrons is only effective in remove energy contri-
 465 bution from nearby charged particles. Nearby neutral particles, predominantly
 466 photons from π^0 decays, also add their energy to the calorimeter clusters, but
 467 mostly in the electromagnetic calorimeter. It is possible to measure this contri-
 468 bution, on average, using late-showering hadrons that minimally ionize in the
 469 electromagnetic calorimeter. Such particles are selected by requiring that they
 470 deposit less than 1.1 GeV in the EM calorimeter within a cone of $\Delta R < 0.1$
 471 around the track. To ensure that these particles are well measured, they are addi-
 472 tionally required to deposit between 40% and 90% of their energy in the hadronic
 473 calorimeter within the same cone.

474 These particle provide a clean sample to measure the nearby neutral back-
 475 ground because they do not deposit energy in the area immediately surrounding
 476 them in the EM calorimeter, as shown in Figure 2. So, the energy deposits in the
 477 region $0.1 < \Delta R < 0.2$ can be attributed to neutral particles alone. To estimate
 478 the contribution to the whole cone considered for the response measurement,
 479 that energy is scaled by a geometric factor of 4/3. This quantity, $\langle E/p \rangle_{\text{BG}}$, mea-
 480 sured in aggregate over a number of particles, gives the contribution to $\langle E/p \rangle$
 481 from neutral particles in the EM calorimeter. Similar techniques were used in
 482 the individual layers of the hadronic calorimeters to show that the background
 483 from neutrals is negligible in those layers [5].

484 The distribution of this background estimate is shown in Figure 5. Although
 485 the simulation captures the overall trend, it significantly overestimates the neu-
 486 tral contribution for tracks with momentum between 2 and 8 GeV. This effect
 487 was also seen in the tails of the E/p distributions in Figure 3. This difference is
 488 likely due to the modeling of coherent neutral particle radiation in Pythia8, as
 489 the discrepancy does not depend on η and thus is unlikely to be a mismodeling
 490 of the detector. This difference can be subtracted to form a corrected average
 491 E/p , as in Section 8.2.4.

492 8.2.4 CORRECTED RESPONSE

493 Figure 6 shows $\langle E/p \rangle_{\text{COR}}$ as a function of momentum for several bins of pseu-
 494 dorapidity. This corrected $\langle E/p \rangle_{\text{COR}} \equiv \langle E/p \rangle - \langle E/p \rangle_{\text{BG}}$ measures the average
 495 calorimeter response without the contamination of neutral particles. It is the
 496 most direct measurement of calorimeter response in that it is the energy mea-
 497 sured for fully isolated hadrons. The correction is performed separately in data
 498 and simulation, so that the mismodeling of the neutral background in simulation
 499 is removed from the comparison of response. The simulation overestimates the
 500 response at low momentum by about 5%, an effect that can be mostly attributed
 501 to the underestimation of the zero fraction mentioned previously.

502 The response measurement above used topological clustering at the EM scale,
 503 that is clusters were formed to measure energy but no corrections were applied
 504 to correct for expected effects like energy lost outside of the cluster or in unin-
 505 strumented material. It is also interesting to measure $\langle E/p \rangle_{\text{COR}}$ using local clus-

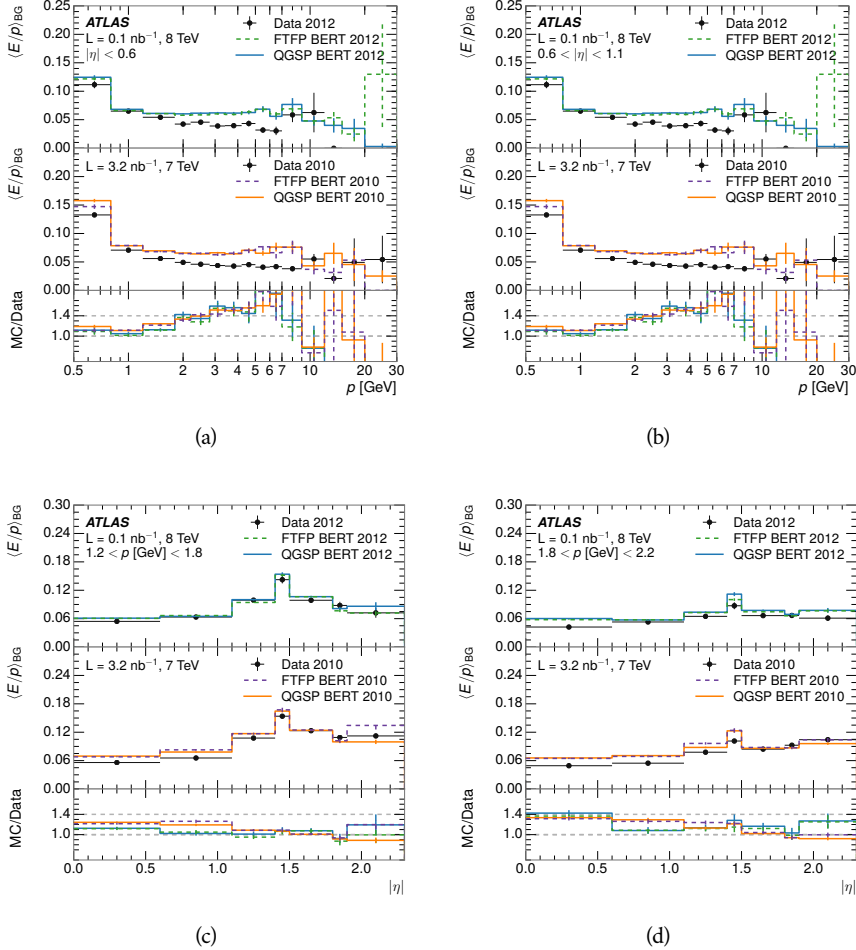


Figure 5: $\langle E/p \rangle_{BG}$ as a function of the track momentum and (a) $|\eta| < 0.6$, (b) $0.6 < |\eta| < 1.1$, and as a function of the track pseudorapidity and (c) $1.2 < p/\text{GeV} < 1.8$, (d) $1.8 < p/\text{GeV} < 2.2$.

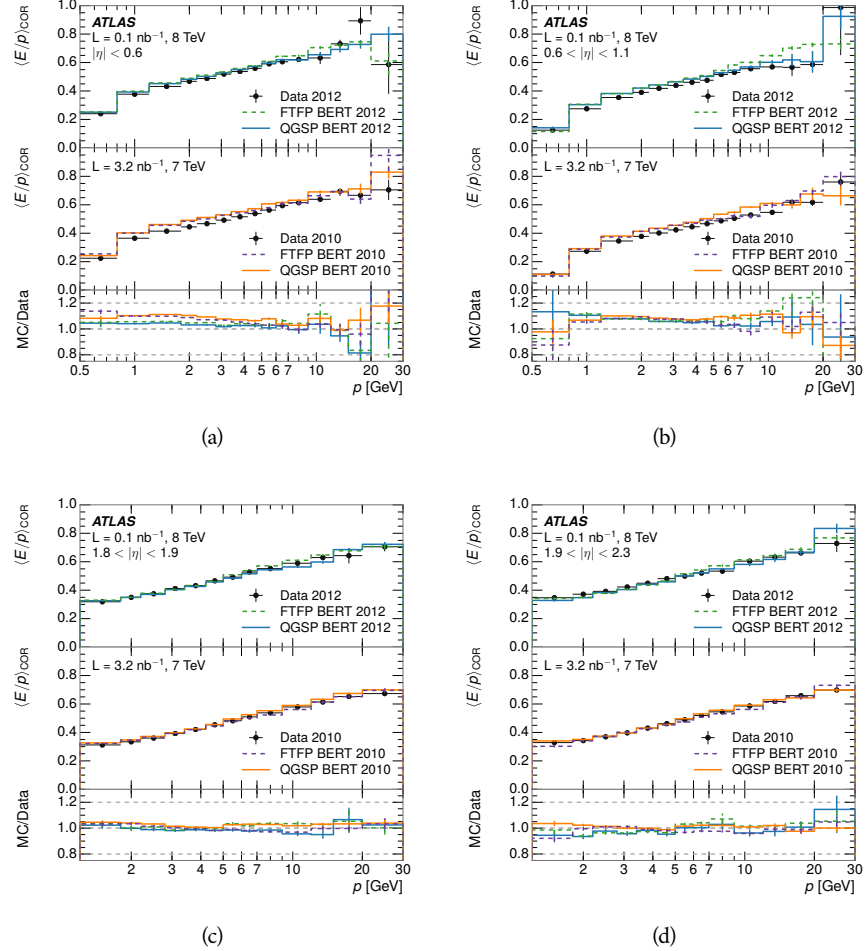


Figure 6: $\langle E/p \rangle_{\text{COR}}$ as a function of track momentum, for tracks with (a) $|\eta| < 0.6$, (b) $0.6 < |\eta| < 1.1$, (c) $1.8 < |\eta| < 1.9$, and (d) $1.9 < |\eta| < 2.3$.

506 ter weighted (LCW) energies, which accounts for those effects by calibrating the
 507 energy based on the properties of the cluster such as energy density and depth
 508 in the calorimeter. Figure 7 shows these distributions for tracks with zero or
 509 more clusters and separately for tracks with one or more clusters. The calibra-
 510 tion moves $\langle E/p \rangle_{\text{COR}}$ significantly closer to 1.0, which is the purpose of the cali-
 511 bration. The agreement between data and simulation improves noticeably when
 512 at least one cluster is required, as this removes the contribution from the mis-
 513 modeling of zero fraction.

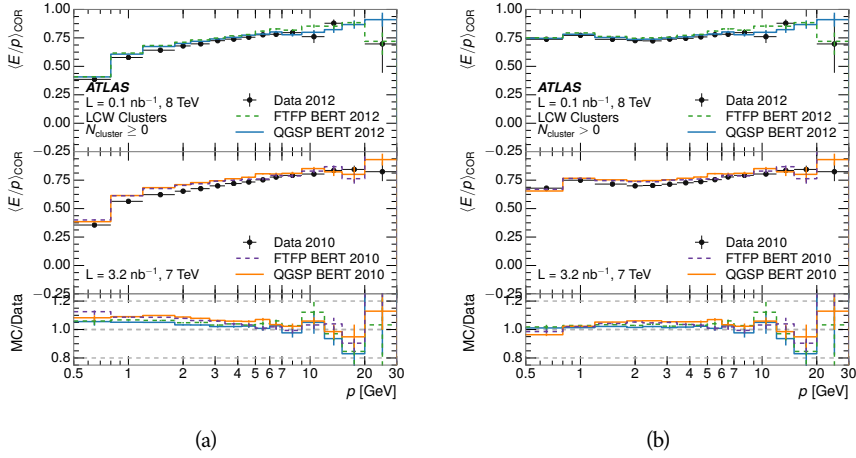


Figure 7: $\langle E/p \rangle_{\text{COR}}$ calculated using LCW-calibrated topological clusters as a function of track momentum for tracks with (a) zero or more associated topological clusters or (b) one or more associated topological clusters.

514 8.2.4.1 ADDITIONAL STUDIES

515 As has been seen in several previous measurements, the simulation does not
 516 correctly model the chance of a low momentum hadron to reach the calorime-
 517 ter. Because of the consistent discrepancy across pseudorapidity and interaction
 518 lengths, this seems to be best explained by incomplete understanding of hadronic
 519 interactions with the detector. For example, a hadron that scatters off of a nu-
 520 cleus in the inner detector can be deflected through a significant angle and not
 521 reach the expected location in the calorimeter. In addition, these interaction can
 522 produce secondary particles that are difficult to model.

523 The requirement on the number of hits in the TRT reduces these effects by
 524 preferentially selecting tracks that do not undergo nuclear interactions. It is in-
 525 teresting to check how well the simulation models tracks with low numbers of
 526 TRT hits, where the nuclear interactions are much more likely. Figure 8 com-
 527 pares the distributions with $N_{\text{TRT}} < 20$ to $N_{\text{TRT}} > 20$ for real and simulated
 528 particles. As expected, the tracks with fewer hits are poorly modeled in the sim-
 529 ulation as $\langle E/p \rangle_{\text{COR}}$ differs by as much as 25% at low momentum.

530 Another interesting aspect of the simulation is the description of antiprotons
 531 at low momentum, where QGSP_BERT and FTFP_BERT have significant differ-
 532 ences. This can be seen to have an effect in the inclusive response measurement

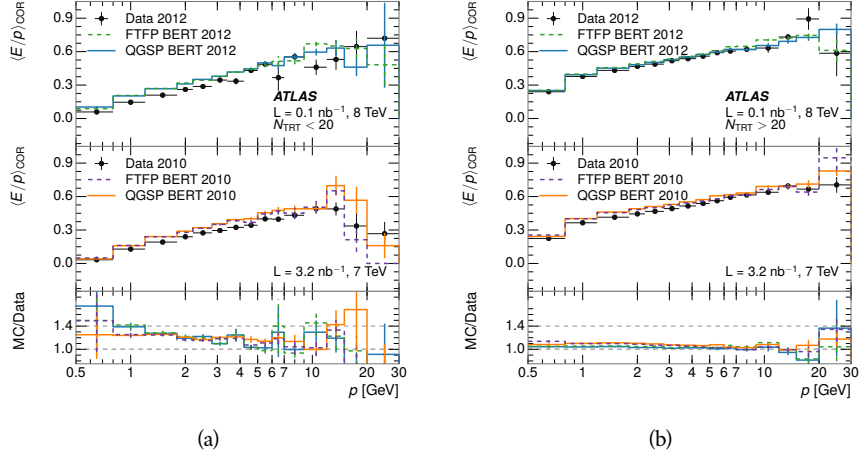


Figure 8: Comparison of the $\langle E/p \rangle_{\text{COR}}$ for tracks with (a) less than and (b) greater than 20 hits in the TRT.

when separated into positive and negative charge. The $\langle E/p \rangle_{\text{COR}}$ distributions for positive and negative particles are shown in Figure 9, where a small difference between QGSP_BERT and FTFP_BERT can be seen in the distribution for negative tracks. This is demonstrated more clearly in Figure 10, which shows the E/p distribution in the two simulations separated by charge. There is a clear difference around $E/p > 1.0$, which can be explained by the additional energy deposited by the annihilation of the antiproton in the calorimeter that is modelled only in FTFP_BERT. This is also explored with data using identified antiprotons in Section 8.3.

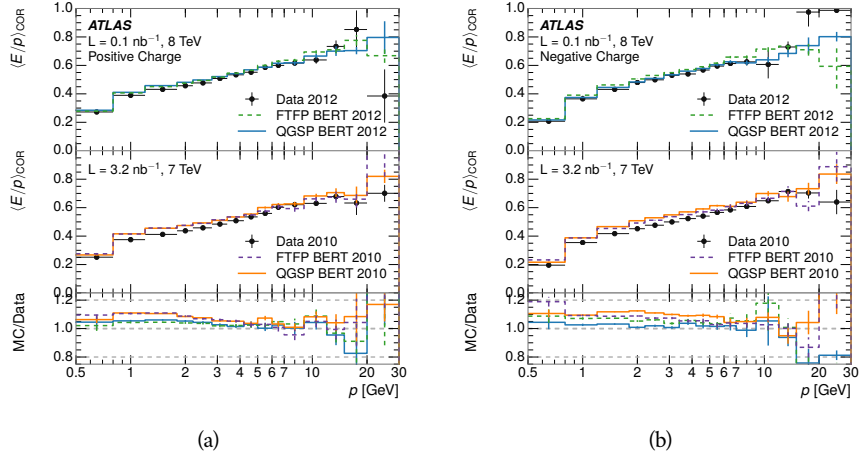


Figure 9: Comparison of the $\langle E/p \rangle_{\text{COR}}$ for (a) positive and (b) negative tracks as a function of track momentum for tracks with $|\eta| < 0.6$.

NOTE: There are more studies that I skipped for brevity that could be included if interesting. E/p in each calorimeter separately, E/p at different cluster threshold settings, E/p with pileup. I also left out a lot of eta bins

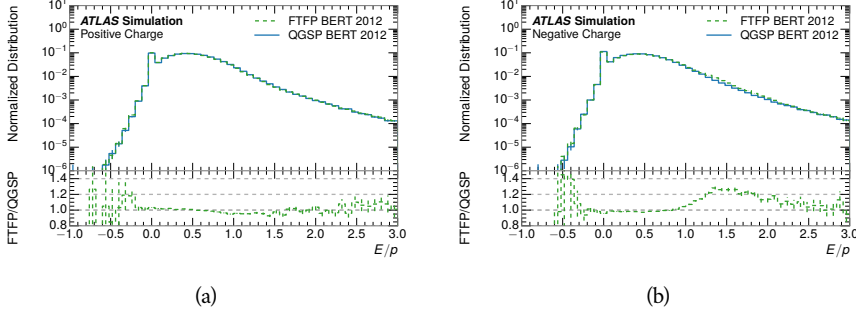


Figure 10: Comparison of the E/p distributions for (a) positive and (b) negative tracks with $0.8 < p/\text{GeV} < 1.2$ and $|\eta| < 0.6$, in simulation with the FTFP_BERT and QGSP_BERT physics lists.

545 **that appear in the paper so that this section didn't turn into 20 pages of
546 plots.**

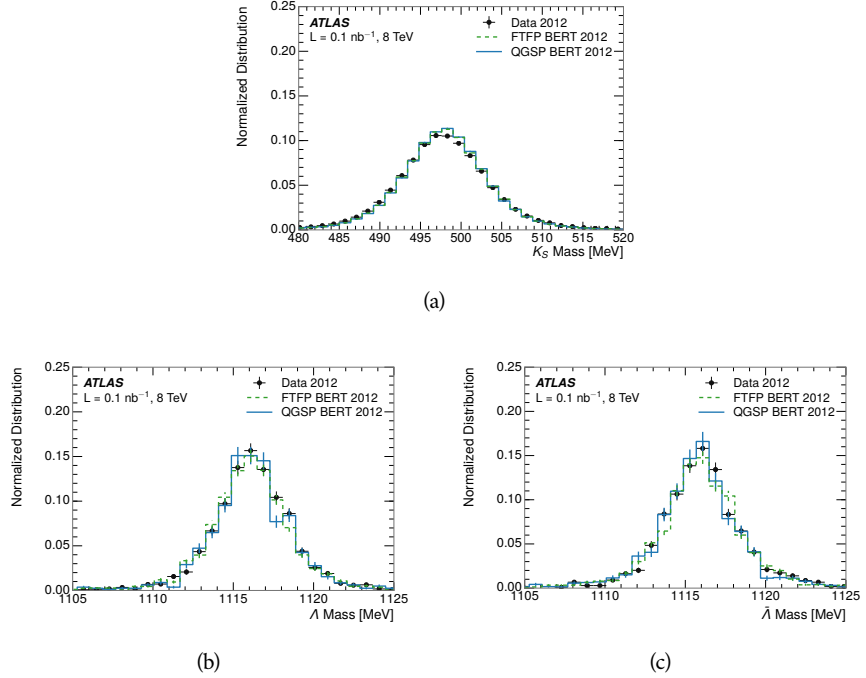
547 8.3 IDENTIFIED PARTICLE RESPONSE

548 The inclusive response measurement for hadrons can be augmented by measur-
549 ing the response for specific particle species. The simulation models each parti-
550 cle type separately, and understanding the properties of each is important in con-
551 straining the uncertainty on jets. In order to select and measure specific hadrons,
552 this section relies on the displaced decays of long-lived particles. Such decays can
553 be identified by reconstructing secondary vertices, and the particles used decay
554 predominantly to specific hadrons. In particular, Λ , $\bar{\Lambda}$, and K_S^0 can be used to
555 select a pure sample of protons, antiprotons, and pions, respectively.

556 8.3.1 DECAY RECONSTRUCTION

557 The measurement of response for identified particles uses the same selection
558 as for inclusive particles (Section 8.1.3, with a few additions. Each event used
559 is required to have at least one secondary vertex, and the tracks are required
560 to match to that vertex rather than the primary vertex. Pions are selected from
561 decays of $K_S^0 \rightarrow \pi^+ \pi^-$, which is the dominant decay for K_S^0 to charged particles.
562 Protons are selected from decays of $\Lambda \rightarrow \pi^- p$ and antiprotons from $\bar{\Lambda} \rightarrow \pi^+ \bar{p}$,
563 which are similarly the dominant decays of Λ and $\bar{\Lambda}$ to charged particles. The
564 species of parent hadron in these decays is determined by reconstructing the
565 mass of the tracks associated to the secondary vertex. The sign of the higher
566 momentum decay particles can distinguish between Λ and $\bar{\Lambda}$, which of course
567 have the same mass, as the proton or antiproton is kinematically favored to have
568 higher momentum. Examples of the reconstructed masses used to select these
569 decays are shown in Figure 11.

570 There are a number of sources of backgrounds for these identified particles,
571 including nuclear interactions and combinatoric sources. These are suppressed

Figure 11: The reconstructed mass peaks of (a) K_S^0 , (b) Λ , and (c) $\bar{\Lambda}$ candidates.

572 by the kinematic requirements on the tracks as well as an additional veto which
 573 removes candidates that are consistent with both a Λ or $\bar{\Lambda}$ and a K_S^0 hypothesis,
 574 which is possible because of the different assumptions on particle mass in each
 575 case [5]. After these requirements, the backgrounds are found to be negligible
 576 compared to the statistical errors on these measurements.

577 8.3.2 IDENTIFIED RESPONSE

578 With these techniques the E/p distributions are extracted in data and simulation
 579 for each particle species and shown in Figure 12. These distributions are shown
 580 for a particular bin of E_a ($2.2 < E_a/\text{GeV} < 2.8$), rather than p . E_a is the energy
 581 available to be deposited in the calorimeter: for pions $E_a = \sqrt{p^2 + m^2}$, for pro-
 582 tons $E_a = \sqrt{p^2 + m^2} - m$, and for antiprotons $E_a = \sqrt{p^2 + m^2} + m$. The features
 583 of the E/p distributions are similar to the inclusive case. There is a small nega-
 584 tive tail from noise and a large fraction of tracks with zero energy from tracks
 585 which do not reach the calorimeter. The long positive tail is noticeably more
 586 pronounced for antiprotons because of the additional energy generated by the
 587 annihilation in addition to the neutral background.

588 The zero fraction is further explored in Figure 13 for pions and protons in
 589 data and simulation. The simulation consistently underestimates the zero frac-
 590 tion independent of particle species, which implies that this discrepancy is not
 591 caused by the model of a particular species but rather a feature common to all.

592 It is also interesting to compare the response between the different particle
 593 species. One approach to do this is to measure the difference in $\langle E/p \rangle$ between
 594 two types, which has the advantage of removing the neutral background. These

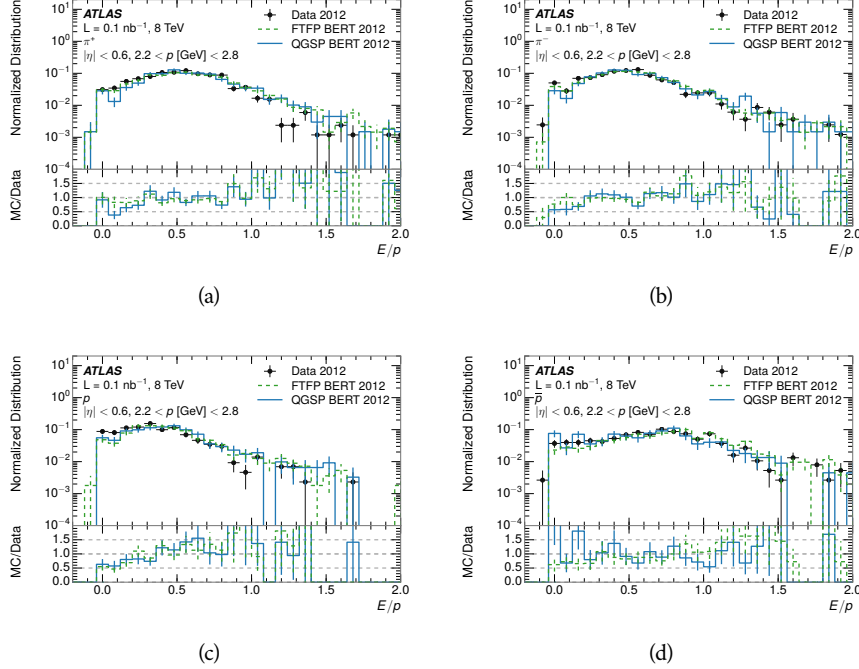


Figure 12: The E/p distribution for isolated (a) π^+ , (b) π^- , (c) proton, and (d) anti-proton tracks.

differences are shown in various combinations in Figure 14. The response for π^+ is greater on average than the response to π^- because of a charge-exchange effect which causes the production of additional neutral pions in the showers of π^+ [20]. The response for π^+ is also greater on average than the response to p , because a large fraction of the energy of π^+ hadrons is converted to an electromagnetic shower [11, 25]. However, the \bar{p} response is significantly higher than the response to π^- , again because of the annihilation of the antiproton. FTFP_BERT does a better job of modeling this effect than QGSP_BERT because of their different descriptions of \bar{p} interactions with material.

It is also possible to remove the neutral background from these response distributions using the same technique as in Section 8.2.3. The technique is largely independent of the particle species and so can be directly applied to $\langle E/p \rangle$ for pions. The $\langle E/p \rangle_{\text{COR}}$ distributions for pions are shown in Figure 15, which are very similar to the inclusive results. The inclusive hadrons are compromised mostly of pions, so this similarity is not surprising. It is also possible to see the small differences between π^+ and π^- response here, where $\langle E/p \rangle_{\text{COR}}$ is higher on average for π^+ . The agreement between data and simulation is significantly worse for the π^- distributions than for the π^+ , with a discrepancy greater than 10% below 2-3 GeV.

8.3.3 ADDITIONAL SPECIES IN SIMULATION

The techniques above provide a method to measure the response separately only pions and protons. However the hadrons which forms jets include a number of

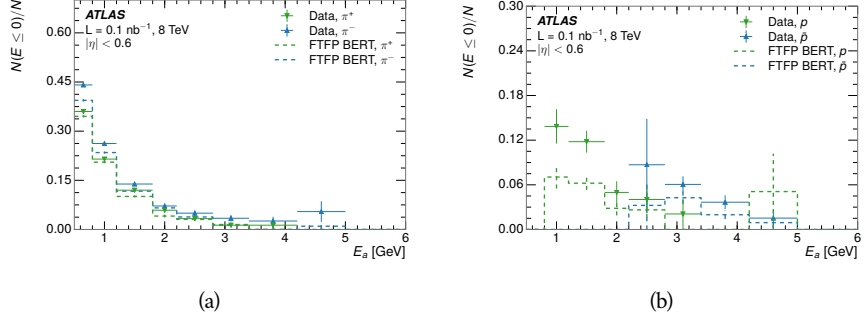


Figure 13: The fraction of tracks with $E \leq 0$ for identified (a) π^+ and π^- , and (b) proton and anti-proton tracks

additional species such as kaons and neutrons. The charged kaons are an important component of the inclusive charged hadron distribution, which is compromised of roughly 60-70% pions, 15-20% kaons, and 5-15% protons. These are difficult to measure in data at the ATLAS detector, although a template subtraction technique has been proposed which may be effective with larger sample sizes [8]. The simulation of these particles includes noticeable differences in response at low energies, which are shown in Figure 16 for FTFP_BERT. The significant differences in response between low energy protons and antiprotons are accounted for above in the definitions of E_a .

626 8.4 SUMMARY

These various measurements of calorimeter response shown above for data and simulation illuminate the accuracy of the simulation of hadronic interactions at the ATLAS detector. The results were done using 2010 and 2012 data at 7 and 8 TeV, but reflect the most current understanding of the detector alignment and geometry. A number of measurements focusing on a comparison between protons and antiprotons suggest that FTFP_BERT models those interaction more accurately than QGSP_BERT. These measurements, among others, were the motivation to switch the default Geant4 simulation from FTFP_BERT to QGSP_BERT for all ATLAS samples.

Even with these updates, there are a number of small, approximately 5%, discrepancies in response between the data and simulation at low energies. At higher energies the simulation of hadronic interactions is very consistent with data. Chapter 9 discusses how to use these observed differences to constrain the jet energy scale and its associated uncertainties.

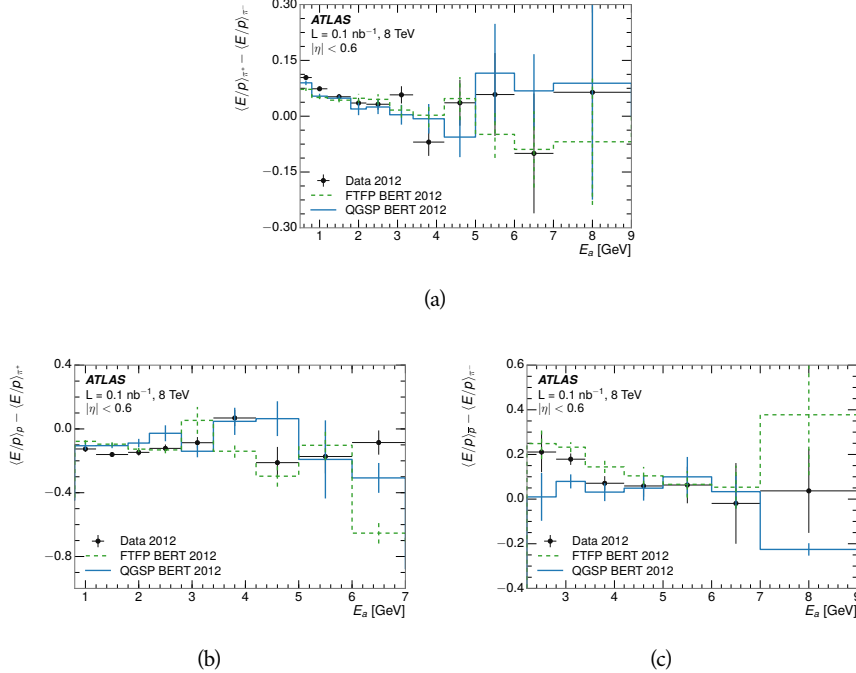


Figure 14: The difference in $\langle E/p \rangle$ between (a) π^+ and π^- (b) p and π^+ , and (c) \bar{p} and π^- .

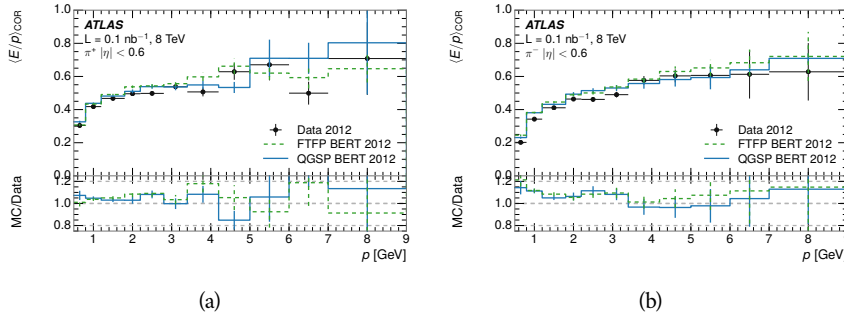


Figure 15: $\langle E/p \rangle_{\text{COR}}$ as a function of track momentum for (a) π^+ tracks and (b) π^- tracks.

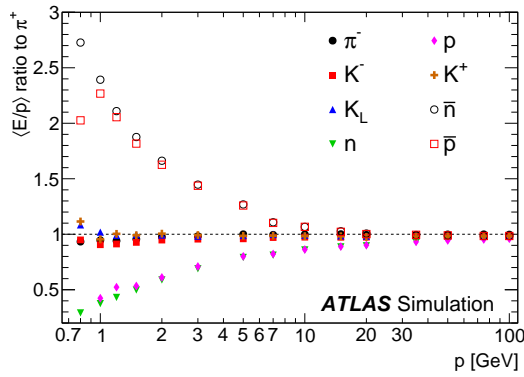


Figure 16: The ratio of the calorimeter response to single particles of various species to the calorimeter response to π^+ with the physics list FTFP_BERT.

641

642 JET ENERGY RESPONSE AND UNCERTAINTY

643 9.1 JET COMPOSITION

644 Dijet and multijet balance techniques provide a method to constrain the jet en-
 645 ergy scale and its uncertainty in data, and provide the default values used for
 646 ATLAS jet measurements at most energies [7]. These techniques are limited by
 647 their reliance on measuring jets in data, so they are statistically limited in estimat-
 648 ing the jet energy scale at the highest jet energies. This chapter presents another
 649 method for estimating the jet energy scale and its uncertainty which builds up a
 650 jet from its components and thus can be naturally extended to high jet momen-
 651 tum. Throughout this chapter the jets studied are simulated using Pythia8 with
 652 the CT10 parton distribution set [27] and the AU2 tune [3], and corrections are
 653 taken from the studies including data and simulation in Chapter 8.

654 As described in Section 7.2, jets are formed from topological clusters of energy
 655 in the calorimeters using the anti- k_t algorithm. These clusters originate from a
 656 diverse spectrum of particles, in terms of both species and momentum, leading to
 657 significantly varied jet properties and response between jets of similar produced
 658 momentum. Figure 17 shows the simulated distribution of particles within jets
 659 at a few examples energies.

660 9.2 UNCERTAINTY ESTIMATE

661 Simulated jets are not necessarily expected to correctly model the energy de-
 662 posits in the calorimeters, because of the various discrepancies discussed in Chap-
 663 ter 8. To evaluate a jet energy response, the simulated jet energies are compared
 664 to a corrected jet built up at the particle level. Each cluster is associated to the
 665 truth particle which deposited it, and the energy in that cluster is then corrected
 666 for a number of effects based on measurements in data. The primary corrections
 667 come from the single hadron response measurements in addition to response
 668 measured using the combined test beam which covers higher momentum parti-
 669 cles [10]. These corrections include both a shift, in order to make the simulation
 670 match the average response in data, and an uncertainty associated with the abil-
 671 ity to constrain the difference between data and simulation. Some of the dom-
 672 inant sources of uncertainty are itemized below, and the full list considered is
 673 described in detail in the associated paper [8]. These uncertainties cover differ-
 674 ences between the data and simulation in the modeling of calorimeter response
 675 to a given particle. No uncertainties are added for the difference between particle
 676 composition of jets in data and simulation.

- 677 • The comparison of $\langle E/p \rangle_{\text{COR}}$ as described in Chapter 8 with statistical
 678 uncertainties from 500 MeV to 20 GeV (“In situ E/p ”).

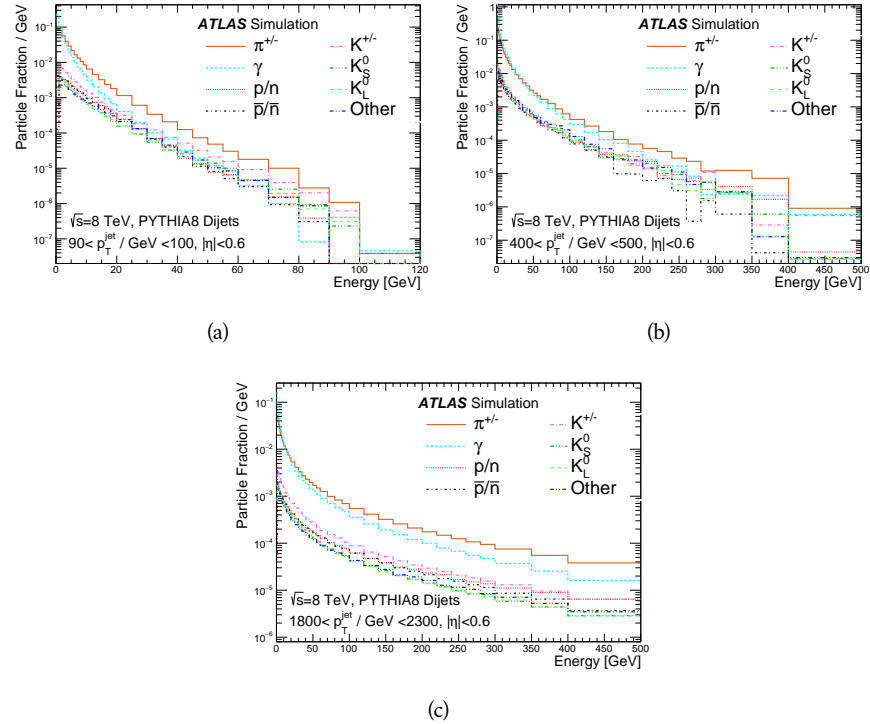
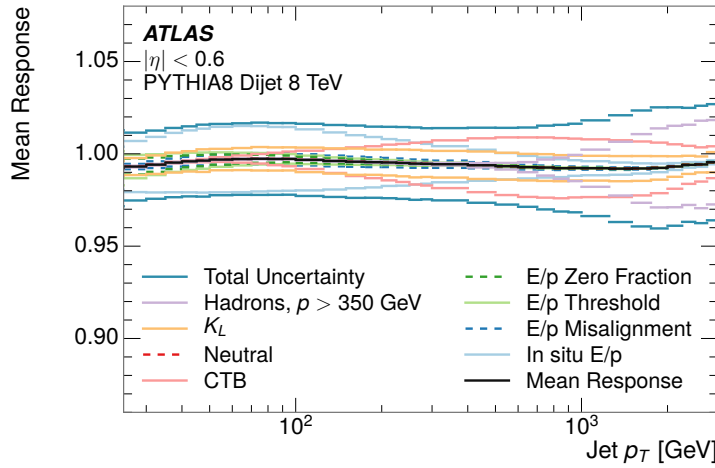


Figure 17: The spectra of true particles inside anti- k_t , $R = 0.4$ jets with (a) $90 < p_T/\text{GeV} < 100$, (b) $400 < p_T/\text{GeV} < 500$, and (c) $1800 < p_T/\text{GeV} < 2300$.

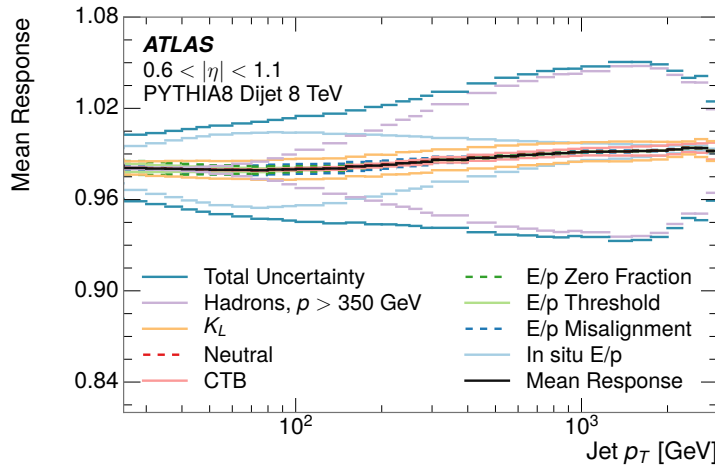
- 679 • The main $\langle E/p \rangle$ comparison uncertainties, binned in p and $|\eta|$, as derived
680 from the combined test beam results, from 20 to 350 GeV (“CTB” from
681 Ref. [10]).
- 682 • The difference in the zero-fraction between data and MC simulation from
683 500 MeV to 20 GeV (“ E/p Zero Fraction”).
- 684 • The uncertainty in the EM calorimeter response from the potential mis-
685 modelling of threshold effects in topological clustering (“ E/p Threshold”).
- 686 • The uncertainty in the calorimeter response to neutral hadrons based on
687 studies of physics model variations (“Neutral”).
- 688 • An additional uncertainty in the response to neutral K_L in the calorimeter
689 based on studies of physics model variations (“ K_L ”).
- 690 • The uncertainty in the p measurement from misalignment of the ID (“ E/p
691 Misalignment”).
- 692 • A flat uncertainty for all particles above the energy range or outside the
693 longitudinal range probed with the combined test beam (included in “Hadrons,
694 $p > 350$ GeV”).

695 From these terms, the jet energy scale and uncertainty is built up from indi-
696 vidual energy deposits in simulation. Each uncertainty term is treated indepen-

697 dently, and are taken to be gaussian distributed. The resulting scale and uncer-
 698 tainty is shown in Figure 18, where the mean response is measured relative to
 699 the calibrated energy reported by simulation. The dominant uncertainties come
 700 from the statistical uncertainties on the E/p measurements at lower energies and
 701 the additional uncertainty for out of range measurements at higher energies. The
 702 total uncertainty from this method at intermediate jet energies is comparable to
 703 other simulation-based methods [4] and is about twice as large as in-situ meth-
 704 ods using data [7]. This method is the only one which provides an estimation
 705 above 1.8 TeV, however, and so is still a crucial technique in analyses that search
 706 for very energetic jets.



(a)



(b)

Figure 18: The jet energy scale uncertainty contributions, as well as the total jet energy scale uncertainty, as a function of jet p_T for (a) $|\eta| < 0.6$ and (b) $0.6 < |\eta| < 1.1$.

707 These techniques can also be used to measure the correlation between the
 708 average reconstructed jet momentum in a given bin of p_T and $|\eta|$, where cor-

relations are expected because of a similarity in particle composition at similar energies. Figure 19 shows these correlations, where the uncertainties on jets in neighboring bins are typically between 30% and 60% correlated. The uncertainty on all jets becomes significantly correlated at high energies and larger pseudorapidities, when the uncertainty becomes dominated by the single term reflecting out of range particles.

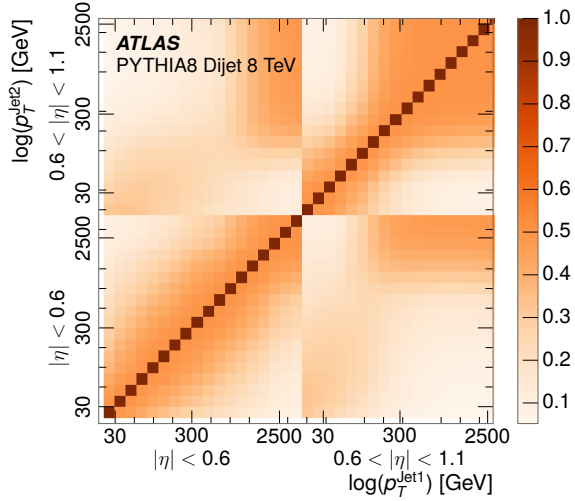


Figure 19: The jet energy scale correlations as a function of jet p_T and $|\eta|$ for jets in the central region of the detector.

9.3 SUMMARY

The technique described above provides a jet energy scale and uncertainty by building up jet corrections from the energy deposits of constituent particles. The E/p measurements are crucial in providing corrections for the majority of particles in the jets. The uncertainty derived this way is between 2 and 5% and is about twice as large at corresponding momentum than jet balance methods. However this is the only uncertainty available for very energetic jets using 2012 data and simulation, and repeating this method with Run 2 data and simulation will be important in providing an uncertainty for the most energetic jets in 13 TeV collisions.

725

PART V

726

SEARCH FOR LONG-LIVED PARTICLES

727

You can put some informational part preamble text here.

10

728

729 LONG-LIVED PARTICLES IN ATLAS

730 10.1 OVERVIEW AND CHARACTERISTICS

731 10.2 SIMULATION

732

733 EVENT SELECTION

734 11.1 TRIGGER

735 11.2 KINEMATICS AND ISOLATION

736 11.3 STANDARD MODEL REJECTION

737 11.4 IONIZATION

738 11.4.1 DE/DX CALIBRATION

739 11.4.2 MASS ESTIMATION

12

740

741 BACKGROUND ESTIMATION

742 12.1 BACKGROUND SOURCES

743 12.2 PREDICTION METHOD

744 12.3 VALIDATION AND UNCERTAINTY

13

745

746 SYSTEMATIC UNCERTAINTIES AND RESULTS

747 13.1 SYSTEMATIC UNCERTAINTIES

748 13.2 FINAL YIELDS

14

749

750 INTERPRETATION

751 14.1 CROSS SECTIONAL LIMITS

752 14.2 MASS LIMITS

753 14.3 CONTEXT FOR LONG-LIVED SEARCHES

754

PART VI

755

CONCLUSIONS

756

You can put some informational part preamble text here.

15

757

758 SUMMARY AND OUTLOOK

759 15.1 SUMMARY

760 15.2 OUTLOOK

761

PART VII

762

APPENDIX

763

A

764

765 INELASTIC CROSS SECTION

B

766

767 APPENDIX TEST

768 Examples: *Italics*, SMALL CAPS, ALL CAPS ¹. Acronym testing: **UML!** (**UML!**) –
769 **UML! – UML! (UML!) – UML!s**

This appendix is temporary and is here to be used to check the style of the document.

770 B.1 APPENDIX SECTION TEST

771 Random text that should take up a few lines. The purpose is to see how sections
772 and subsections flow with some actual context. Without some body copy be-
773 tween each heading it can be difficult to tell if the weight of the fonts, styles,
774 and sizes use work well together.

775 B.1.1 APPENDIX SUBECTION TEST

776 Random text that should take up a few lines. The purpose is to see how sections
777 and subsections flow with some actual context. Without some body copy be-
778 tween each heading it can be difficult to tell if the weight of the fonts, styles,
779 and sizes use work well together.

780 B.2 A TABLE AND LISTING

781 Curabitur tellus magna, porttitor a, commodo a, commodo in, tortor. Donec in-
782 terdum. Praesent scelerisque. Maecenas posuere sodales odio. Vivamus metus la-
783 cus, varius quis, imperdiet quis, rhoncus a, turpis. Etiam ligula arcu, elementum a,
784 venenatis quis, sollicitudin sed, metus. Donec nunc pede, tincidunt in, venenatis
785 vitae, faucibus vel, nibh. Pellentesque wisi. Nullam malesuada. Morbi ut tellus ut
786 pede tincidunt porta. Lorem ipsum dolor sit amet, consectetur adipiscing elit.
787 Etiam congue neque id dolor.

788 There is also a Python listing below Listing 1.

1 Footnote example.

LABITUR BONORUM PRI NO	QUE VISTA	HUMAN
fastidii ea ius	germano	demonstratea
suscipit instructior	titulo	personas
quaestio philosophia	facto	demonstrated

Table 1: Autem usu id.

789 B.3 SOME FORMULAS

Due to the statistical nature of ionisation energy loss, large fluctuations can occur in the amount of energy deposited by a particle traversing an absorber element². Continuous processes such as multiple scattering and energy loss play a relevant role in the longitudinal and lateral development of electromagnetic and hadronic showers, and in the case of sampling calorimeters the measured resolution can be significantly affected by such fluctuations in their active layers. The description of ionisation fluctuations is characterised by the significance parameter κ , which is proportional to the ratio of mean energy loss to the maximum allowed energy transfer in a single collision with an atomic electron:

You might get unexpected results using math in chapter or section heads. Consider the pdfspacing option.

$$\kappa = \frac{\xi}{E_{\max}} \quad (1)$$

E_{\max} is the maximum transferable energy in a single collision with an atomic electron.

$$E_{\max} = \frac{2m_e\beta^2\gamma^2}{1 + 2\gamma m_e/m_x + (m_e/m_x)^2},$$

790 where $\gamma = E/m_x$, E is energy and m_x the mass of the incident particle, $\beta^2 =$
 791 $1 - 1/\gamma^2$ and m_e is the electron mass. ξ comes from the Rutherford scattering
 792 cross section and is defined as:

$$\xi = \frac{2\pi z^2 e^4 N_{Av} Z \rho \delta x}{m_e \beta^2 c^2 A} = 153.4 \frac{z^2}{\beta^2} \frac{Z}{A} \rho \delta x \text{ keV},$$

793 where

z charge of the incident particle
 794 N_{Av} Avogadro's number
 Z atomic number of the material
 A atomic weight of the material
 ρ density
 δx thickness of the material
 795 κ measures the contribution of the collisions with energy transfer close to
 796 E_{\max} . For a given absorber, κ tends towards large values if δx is large and/or if
 797 β is small. Likewise, κ tends towards zero if δx is small and/or if β approaches
 798 1.

2 Examples taken from Walter Schmidt's great gallery:
<http://home.vrweb.de/~was/mathfonts.html>

Listing 1: A floating example (listings manual)

```
1 for i in xrange(10):
    print i, i*i, i*i*i
print "done"
```

799 The value of κ distinguishes two regimes which occur in the description of
800 ionisation fluctuations:

- 801 1. A large number of collisions involving the loss of all or most of the incident
802 particle energy during the traversal of an absorber.

803 As the total energy transfer is composed of a multitude of small energy
804 losses, we can apply the central limit theorem and describe the fluctua-
805 tions by a Gaussian distribution. This case is applicable to non-relativistic
806 particles and is described by the inequality $\kappa > 10$ (i. e., when the mean
807 energy loss in the absorber is greater than the maximum energy transfer
808 in a single collision).

- 809 2. Particles traversing thin counters and incident electrons under any condi-
810 tions.

811 The relevant inequalities and distributions are $0.01 < \kappa < 10$, Vavilov
812 distribution, and $\kappa < 0.01$, Landau distribution.

813 BIBLIOGRAPHY

- 814 [1] ATLAS Collaboration. “The ATLAS Simulation Infrastructure”. In: *Eur.*
815 *Phys. J. C* 70 (2010), p. 823. doi: [10.1140/epjc/s10052-010-1429-9](https://doi.org/10.1140/epjc/s10052-010-1429-9).
816 arXiv: [1005.4568 \[hep-ex\]](https://arxiv.org/abs/1005.4568). SOFT-2010-01.
- 817 [2] ATLAS Collaboration. “A study of the material in the ATLAS inner de-
818 tector using secondary hadronic interactions”. In: *JINST* 7 (2012), P01013.
819 doi: [10.1088/1748-0221/7/01/P01013](https://doi.org/10.1088/1748-0221/7/01/P01013). arXiv: [1110.6191 \[hep-ex\]](https://arxiv.org/abs/1110.6191).
820 PERF-2011-08.
- 821 [3] ATLAS Collaboration. *Summary of ATLAS Pythia 8 tunes*. ATL-PHYS-PUB-
822 2012-003. 2012. url: <http://cds.cern.ch/record/1474107>.
- 823 [4] ATLAS Collaboration. “Jet energy measurement with the ATLAS detector
824 in proton–proton collisions at $\sqrt{s} = 7$ TeV”. In: *Eur. Phys. J. C* 73 (2013),
825 p. 2304. doi: [10.1140/epjc/s10052-013-2304-2](https://doi.org/10.1140/epjc/s10052-013-2304-2). arXiv: [1112.6426 \[hep-ex\]](https://arxiv.org/abs/1112.6426). PERF-2011-03.
- 826 [5] ATLAS Collaboration. “Single hadron response measurement and calorime-
827 ter jet energy scale uncertainty with the ATLAS detector at the LHC”. In:
828 *Eur. Phys. J. C* 73 (2013), p. 2305. doi: [10.1140/epjc/s10052-013-2305-1](https://doi.org/10.1140/epjc/s10052-013-2305-1). arXiv: [1203.1302 \[hep-ex\]](https://arxiv.org/abs/1203.1302). PERF-2011-05.
- 829 [6] ATLAS Collaboration. “Electron and photon energy calibration with the
830 ATLAS detector using LHC Run 1 data”. In: *Eur. Phys. J. C* 74 (2014), p. 3071.
831 doi: [10.1140/epjc/s10052-014-3071-4](https://doi.org/10.1140/epjc/s10052-014-3071-4). arXiv: [1407.5063 \[hep-ex\]](https://arxiv.org/abs/1407.5063). PERF-2013-05.
- 832 [7] ATLAS Collaboration. “Jet energy measurement and its systematic uncer-
833 tainty in proton–proton collisions at $\sqrt{s} = 7$ TeV with the ATLAS detec-
834 tor”. In: *Eur. Phys. J. C* 75 (2015), p. 17. doi: [10.1140/epjc/s10052-014-3190-y](https://doi.org/10.1140/epjc/s10052-014-3190-y). arXiv: [1406.0076 \[hep-ex\]](https://arxiv.org/abs/1406.0076). PERF-2012-01.
- 835 [8] ATLAS Collaboration. “A measurement of the calorimeter response to sin-
836 ggle hadrons and determination of the jet energy scale uncertainty using
837 LHC Run-1 pp -collision data with the ATLAS detector”. In: (2016). arXiv:
838 [1607.08842 \[hep-ex\]](https://arxiv.org/abs/1607.08842). PERF-2015-05.
- 839 [9] ATLAS Collaboration. “Topological cell clustering in the ATLAS calorime-
840 ters and its performance in LHC Run 1”. In: (2016). arXiv: [1603.02934](https://arxiv.org/abs/1603.02934)
841 [hep-ex].
- 842 [10] E. Abat et al. “Study of energy response and resolution of the ATLAS barrel
843 calorimeter to hadrons of energies from 20 to 350 GeV”. In: *Nucl. Instrum.*
844 *Meth. A* 621.1-3 (2010), pp. 134 – 150. doi: <http://dx.doi.org/10.1016/j.nima.2010.04.054>.

- 850 [11] P. Adragna et al. "Measurement of Pion and Proton Response and Lon-
 851 gitudinal Shower Profiles up to 20 Nuclear Interaction Lengths with the
 852 ATLAS Tile Calorimeter". In: *Nucl. Instrum. Meth. A* 615 (2010), pp. 158–
 853 181. doi: [10.1016/j.nima.2010.01.037](https://doi.org/10.1016/j.nima.2010.01.037).
- 854 [12] S. Agostinelli et al. "GEANT4: A simulation toolkit". In: *Nucl. Instrum. Meth.*
 855 A 506 (2003), pp. 250–303. doi: [10.1016/S0168-9002\(03\)01368-8](https://doi.org/10.1016/S0168-9002(03)01368-8).
- 856 [13] N. S. Amelin et al. "Transverse flow and collectivity in ultrarelativistic
 857 heavy-ion collisions". In: *Phys. Rev. Lett.* 67 (1991), p. 1523. doi: [10.1103/PhysRevLett.67.1523](https://doi.org/10.1103/PhysRevLett.67.1523).
- 858 [14] N. S. Amelin et al. "Collectivity in ultrarelativistic heavy ion collisions". In:
 859 *Nucl. Phys. A* 544 (1992), p. 463. doi: [10.1016/0375-9474\(92\)90598-E](https://doi.org/10.1016/0375-9474(92)90598-E).
- 860 [15] B. Andersson, A. Tai, and B.-H. Sa. "Final state interactions in the (nuclear)
 861 FRITIOF string interaction scenario". In: *Z. Phys. C* 70 (1996), pp. 499–
 862 506. doi: [10.1007/s002880050127](https://doi.org/10.1007/s002880050127).
- 863 [16] B. Andersson et al. "A model for low-pT hadronic reactions with general-
 864 izations to hadron-nucleus and nucleus-nucleus collisions". In: *Nucl. Phys.*
 865 B 281 (1987), p. 289. doi: [10.1016/0550-3213\(87\)90257-4](https://doi.org/10.1016/0550-3213(87)90257-4).
- 866 [17] H. W. Bertini and P. Guthrie. "News item results from medium-energy
 867 intranuclear-cascade calculation". In: *Nucl. Instr. and Meth. A* 169 (1971),
 868 p. 670. doi: [10.1016/0375-9474\(71\)90710-X](https://doi.org/10.1016/0375-9474(71)90710-X).
- 869 [18] L. V. Bravin et al. "Scaling violation of transverse flow in heavy ion col-
 870 lisions at AGS energies". In: *Phys. Lett. B* 344 (1995), p. 49. doi: [10.1016/0370-2693\(94\)01560-Y](https://doi.org/10.1016/0370-2693(94)01560-Y).
- 871 [19] L. V. Bravina et al. "Fluid dynamics and Quark Gluon string model - What
 872 we can expect for Au+Au collisions at 11.6 AGeV/c". In: *Nucl. Phys. A* 566
 873 (1994), p. 461. doi: [10.1016/0375-9474\(94\)90669-6](https://doi.org/10.1016/0375-9474(94)90669-6).
- 874 [20] CMS Collaboration. "The CMS barrel calorimeter response to particle
 875 beams from 2 to 350 GeV/c". In: *Eur. Phys. J. C* 60.3 (2009). doi: [10.1140/epjc/s10052-009-0959-5](https://doi.org/10.1140/epjc/s10052-009-0959-5).
- 876 [21] H. S. Fesefeldt. *GHEISHA program*. Pitha-85-02, Aachen. 1985.
- 877 [22] G. Folger and J.P. Wellisch. "String parton models in Geant4". In: (2003).
 878 arXiv: [nucl-th/0306007](https://arxiv.org/abs/nucl-th/0306007).
- 879 [23] B. Ganhuyag and V. Uzhinsky. "Modified FRITIOF code: Negative charged
 880 particle production in high energy nucleus nucleus interactions". In: *Czech.
 881 J. Phys.* 47 (1997), pp. 913–918. doi: [10.1023/A:1021296114786](https://doi.org/10.1023/A:1021296114786).
- 882 [24] M. P. Guthrie, R. G. Alsmiller, and H. W. Bertini. "Calculation of the cap-
 883 ture of negative pions in light elements and comparison with experiments
 884 pertaining to cancer radiotherapy". In: *Nucl. Instrum. Meth.* 66 (1968), pp. 29–
 885 36. doi: [10.1016/0029-554X\(68\)90054-2](https://doi.org/10.1016/0029-554X(68)90054-2).
- 886 [25] J. Beringer et al. (Particle Data Group). "Review of Particle Physics". In:
 887 *Chin. Phys. C* 38 (2014), p. 090001. URL: <http://pdg.lbl.gov>.

- 892 [26] V.A. Karmanov. "Light Front Wave Function of Relativistic Composite
893 System in Explicitly Solvable Model". In: *Nucl. Phys. B* 166 (1980), p. 378.
894 doi: [10.1016/0550-3213\(80\)90204-7](https://doi.org/10.1016/0550-3213(80)90204-7).
- 895 [27] Hung-Liang Lai, Marco Guzzi, Joey Huston, Zhao Li, Pavel M. Nadolsky,
896 et al. "New parton distributions for collider physics". In: *Phys. Rev. D* 82
897 (2010), p. 074024. doi: [10.1103/PhysRevD.82.074024](https://doi.org/10.1103/PhysRevD.82.074024). arXiv: [1007.2241 \[hep-ph\]](https://arxiv.org/abs/1007.2241).
- 898 [28] A.D. Martin, W.J. Stirling, R.S. Thorne, and G. Watt. "Parton distributions
899 for the LHC". In: *Eur. Phys. J. C* 63 (2009). Figures from the [MSTW Website](#),
900 pp. 189–285. doi: [10.1140/epjc/s10052-009-1072-5](https://doi.org/10.1140/epjc/s10052-009-1072-5). arXiv: [0901.0002](https://arxiv.org/abs/0901.0002).
- 901 [29] B. Nilsson-Almqvist and E. Stenlund. "Interactions Between Hadrons and
902 Nuclei: The Lund Monte Carlo, Fritiof Version 1.6". In: *Comput. Phys. Com-
903 mun.* 43 (1987), p. 387. doi: [10.1016/0010-4655\(87\)90056-7](https://doi.org/10.1016/0010-4655(87)90056-7).
- 904 [30] A. Ribon et al. *Status of Geant4 hadronic physics for the simulation of LHC
905 experiments at the start of LHC physics program*. CERN-LCGAPP-2010-02.
906 2010. URL: <http://lcgapp.cern.ch/project/docs/noteStatusHadronic2010.pdf>.
- 907 [31] A. Sherstnev and R.S. Thorne. "Parton Distributions for LO Generators".
908 In: *Eur. Phys. J. C* 55 (2008), pp. 553–575. doi: [10.1140/epjc/s10052-008-0610-x](https://doi.org/10.1140/epjc/s10052-008-0610-x). arXiv: [0711.2473](https://arxiv.org/abs/0711.2473).
- 909 [32] T. Sjöstrand, S. Mrenna, and P. Skands. "A Brief Introduction to PYTHIA
910 8.1". In: *Comput. Phys. Commun.* 178 (2008), pp. 852–867. doi: [10.1016/j.cpc.2008.01.036](https://doi.org/10.1016/j.cpc.2008.01.036). arXiv: [0710.3820](https://arxiv.org/abs/0710.3820).
- 911 [33] Peter Speckmayer. "Energy Measurement of Hadrons with the CERN AT-
912 LAS Calorimeter". Presented on 18 Jun 2008. PhD thesis. Vienna: Vienna,
913 Tech. U., 2008. URL: <http://cds.cern.ch/record/1112036>.

919 DECLARATION

920 Put your declaration here.

921 *Berkeley, CA, September 2016*

922

Bradley Axen

923

924 COLOPHON

925

Not sure that this is necessary.